

Contents lists available at ScienceDirect

Journal of the Mechanics and Physics of Solids

journal homepage: www.elsevier.com/locate/jmps



Rate dependent adhesion of nanoscale polymer contacts



Debashish Das, Ioannis Chasiotis *

Aerospace Engineering, University of Illinois at Urbana-Champaign, Urbana, IL, USA

ARTICLE INFO

Keywords:
Maugis-Dugdale
JKR
Surface energy
van der Waals
Viscoelasticity
Nanofibers

ABSTRACT

The adhesive interactions between polymer nanofibers strongly influence the mechanical behavior of their networks in synthetic materials and biological systems. A treatment of the adhesive interactions at polymer contacts must take into account the viscoelastic behavior of the material in the contact region and the associated energy dissipation. This study focuses on the rate-dependent adhesion of polyacrylonitrile (PAN) nanofibers which interact with strong van der Waals forces. Experimental measurements of the detachment force between PAN fibers with diameters 400 and 4000 nm showed that the apparent work of adhesion increases with the rate of unloading by a factor of two within a three orders of magnitude increase in the unloading rate. In order to obtain further insights into this rate-dependent adhesion, the Maugis-Dugdale (M-D) elastic contact model for normal detachment was extended to include a linear viscoelastic behavior of the PAN nanofibers. The extended model predicted the normal pull-off force instabilities in good agreement with the experiments, capturing well the effect of the unloading rate. The calculated viscoelastic time constants were of the order of milliseconds, suggesting fast relaxations in the contact region, which explain the instantaneous full-strength reattachment of nanoscale polymer fibers during slip-stick experiments.

1. Introduction

The adhesion between soft nanoscale fibers plays a significant role in the deformation mechanics of engineered nanofiber networks, fibrous biological structures, and their respective composites (Negi and Picu, 2019). Compared to macroscale soft material structures, the effect of adhesion is more pronounced at the micro and the nanometer length scales because of the significantly larger surface-to-volume ratio. In a perfectly elastic material, the process of loading and unloading is reversible and contact mechanics models such as the Johnson-Kendall-Roberts (JKR) (Johnson et al., 1971), the Maugis-Dugdale (M-D) (Maugis, 1992), or the Derjaguin-Muller-Toporov (DMT) (Derjaguin et al., 1975) model have been applied in the past to extract the work of adhesion. However, polymeric materials are viscoelastic, hence demonstrating adhesion hysteresis, due to which the work done to separate two adhering surfaces is not fully recovered when the two surfaces are brought back into contact (Maeda et al., 2002; Waters and Guduru, 2010), because during separation there is viscoelastic dissipation of a fraction of the work done by external forces. When two surfaces are brought together, the surface energy provides the driving force to overcome dissipation, as well as the external work. Thus, the external work needed to separate two surfaces exceeds the energy that is returned when the surfaces come together, due to internal dissipation. In addition, the apparent work of adhesion has been observed to be rate dependent when two surfaces separate or adhere. This energy dissipation (Liu et al., 2018) and rate-dependency (Naraghi et al., 2014) in polymers is due to time-dependent molecular

E-mail address: chasioti@illinois.edu (I. Chasiotis).

^{*} Corresponding author.

chain-level rearrangement processes that manifest as macroscale viscoelastic behavior. Macroscale normal detachment experiments of glass (Maugis and Barquins, 1978) and silicon nitride (Lorenz et al., 2013) spheres from polyurethane and PDMS elastomeric films, respectively, have shown that the apparent work of adhesion increases with the peeling rate (or crack tip velocity). For instance, Zeng et al. (2006) performed pull-off experiments on thin polystyrene films attached to mica cylinders and showed that even at the micrometer length scales, the pull-off force, and thus the apparent surface energy, increases with the separation rate following an S-shaped growth curve.

In the absence of adhesion, the linear viscoelastic contact problem of spheres has been studied in detail by Ting (1966) and Graham (1967). Later, Maugis and Barquins (1978) used linear elastic fracture mechanics (LEFM) to generalize the mechanics of adhesion of elastic bodies, and experimentally showed that the effective work of adhesion required to separate two adhering objects was a function of the rate of peeling. A relevant solution to the problem of crack propagation and healing in viscoelastic materials was provided earlier by Schapery (1975), (1975) and (1989). Contrary to elastic materials, during crack growth in viscoelastic materials the energy flowing from the far field to the crack tip is affected by energy dissipation, thus, making the available energy for crack growth a quantity that needs to be determined. Therefore, although the reversible elastic problem (where loading and unloading contact size vs. normal load data are identical) is completely described by the work of adhesion (i.e., the total work done by the adhesive forces), the problem of crack growth in viscoelastic materials requires additional information about the distribution of the adhesive forces in order to develop a thorough description. For a growing crack in a viscoelastic medium, the material near the crack tip would experience an "infinite" strain rate due to the singular stress field associated with a JKR type model (because of negligible cohesive zone length), and as a result, there can be no dissipation or crack velocity dependence on the propagation of the crack. In contrast, introducing a cohesive zone with a finite size over which the interaction stresses act, leads to a finite strain rate resulting in velocity dependent dissipation (Hui et al., 1998; Barthel and Frétigny, 2009). Hence, models that consider a simple distribution of adhesive forces, such as the Dugdale (1960) and Barenblatt (1962) or the double-Hertz (Greenwood and Johnson, 1998) cohesive-zone models, have been successful in describing viscoelastic crack growth. Cohesive-zone crack modeling has been used, for example by Liechti and Wu (2001), to simulate crack propagation in rubber-metal debonding. The authors introduced a rate-dependent traction-separation law at the rubber-metal interface along with a rate-dependent bulk rubber behavior to model quasi-static debonding under opening and mixed-mode loading conditions. The results in Liechti and Wu (2001) highlighted the need to introduce rate-dependence in the cohesive zone.

Consideration of the aforementioned time-dependent processes in adhesive contacts at the micron and the nanometer length scales is further restricted by the lack of experimental data, stemming from inherent difficulties in conducting experiments at these length scales and actually measuring the geometry of the contact. The majority of the few existing studies focus on the normal detachment problem of two nanofibers at a single detachment rate (Das and Chasiotis, 2020; Shi et al., 2010; Stachewicz et al., 2014; Wang et al., 2012, 2017). Only one experimental study (Shi et al., 2012) has delved into the effect of the detachment rate on the "pull-off" force between polycaprolactone microfibers, showing an increase in the work of adhesion with increasing detachment rate, albeit in a quite narrow range of applied detachment rates. However, for meaningful conclusions to be drawn, such experimental results need to be put in a theoretical framework that incorporates the effect of viscoelasticity on the adhesive response.

This combined experimental and analytical study focuses on the role of time-dependent material processes in the apparent work of adhesion between polymeric nanofibers interacting through strong van der Waals forces. The experimental method allows for a broad spectrum of detachment rates and contact displacements, bridging limit cases in rate-dependent normal detachment response. A theoretical framework using the M-D model combined with LEFM and linear viscoelasticity provides the background to analyze the experimental results, quantify the relevant material time scales at the fiber contact, and make predictions for the apparent work of adhesion as a function of detachment rate.

2. Materials and methods

Nanoscale contact experiments were carried out with polyacrylonitrile (PAN) nanofibers. The latter were selected because of the high surface energy of PAN (Das and Chasiotis, 2020) which during cold drawing deforms homogeneously without strain localization and necking (Naraghi et al., 2007). The PAN nanofibers were synthesized via electrospinning from N, N-dimethylformamide (DMF) solutions of 9, 12, and 15 wt.% PAN powders with MW=150,000 g/mol (Sigma–Aldrich). The PAN powders were dissolved in DMF at room temperature through constant stirring for 24 h. The electrospinning voltage and the distance to the collector were 25 kV and 25 cm, respectively, at a relative humidity of 17% which was maintained inside a chamber by using calcium sulfate as desiccant. PAN nanofibers with uniform diameter along their length were spun in suspended form on a wireframe collector and subsequently annealed at 105 °C (20 °C above the glass transition temperature, T_g) for 2 h to remove the surface roughness and any residual solvent (Das and Chasiotis, 2020). The fiber diameter was controlled by the concentration of the polymer solution. Higher polymer concentrations increased the solution viscosity and limited the stretching effect of the electrostatic repulsion forces, hence resulting in fibers with larger diameters (Das and Chasiotis, 2020). Two extreme cases of PAN fibers were explored in this study, with diameters of 380 nm and 4100 nm.

Measurements of the adhesion force between individual PAN nanofibers were conducted in ambient conditions (23°C, 20–50% relative humidity) by using a Microelectromechanical Systems (MEMS) type device under a high magnification optical microscope. Due to the sensitive nature of the polymer nanofibers, *in-situ* tests inside a Scanning Electron Microscope (SEM) are prohibitive. Instead, the optical microscopy method developed for this study allowed for fast imaging via a high-speed digital camera with frame rates as high as 30,000 fps to record high magnification optical images during fast testing. Then, Digital Image Correlation (DIC) was applied post-mortem to the optical images of the test device with the attached nanofiber, Fig. 1, to calculate the relative motion of the components of the MEMS device and thus derive the applied force on the fibers (Naraghi et al., 2010; Naraghi et al., 2007) with a

Fig. 1. (a) PAN nanofiber mounted on a MEMS device. (b) Schematic of a normal detachment test in which two fibers are brought at a slow rate into adhesive contact in crossed-cylinder geometry, pressed into contact for 15 min, and subsequently pulled apart at various crosshead velocities.

resolution of \sim 2 nN or better depending on the stiffness of the MEMS device (Das and Chasiotis, 2020). For each normal detachment test, two PAN fiber segments were isolated from the same fiber with the aid of a micromanipulator and each segment was mounted across a 50 μ m section of a different MEMS device using a two-part epoxy, Fig. 1(a). Using fibers with the same diameter ensures a circular contact area (Das and Chasiotis, 2020). Fig. 1(b) shows a schematic of the normal detachment procedure, where the midpoints of two orthogonally positioned fibers are pressed into contact, held for 15 min in compression, and then pulled apart. The MEMS device on the right was translated with a piezoelectric actuator at nominal speeds ranging between 3 nms⁻¹ and 1 mms⁻¹. Note that the contact point was in the middle of each fiber to prevent the moments arising from resultant tension components. The fiber diameter was measured via an SEM after completion of all measurements.

3. Results and discussion

3.1. Normal detachment experiments

Fig. 2(a) shows a typical holding-unloading trajectory during a normal detachment test at a constant crosshead velocity of $2 \, \mu ms^{-1}$. In the approach phase, the fibers were brought towards each other at 12 nms⁻¹. A snap-in instability took place when the effective spring constant of the force sensor and the fiber segments became equal to the gradient of the force-distance curve, e.g. (Das and Chasiotis, 2020). Further compression bent and stretched the fibers to an initial compressive preload of 40 ± 20 nN and 650 ± 300 nN for the 380 nm and 4100 nm diameter fibers, respectively, which was maintained for 15 min before the detachment (unloading) process began. As a test of the effect of preload on the normal detachment force, Fig. 2(b) shows that the detachment force does not depend appreciably on the initial compressive preload: the pull-off forces between two 3450 nm diameter fibers lie in a narrow range, 1472 ± 50 nN, for initial compressive preloads varying between 130-3000 nN and a fixed crosshead velocity of $2 \mu ms^{-1}$. It will be further shown in Section 3.5 that the same result can also be obtained numerically. During unloading, the two fibers detach when a tensile pull-off force is reached. The experimental unloading trajectory provides the pull-off force and the unloading rate, dP/dt as shown in Fig. 2(a). In the beginning the unloading rate is not constant due to bending and stretching of the fibers, but it assumes a constant value at the later part of the unloading process, Fig. 2(a). Different nominal crosshead velocities provided different unloading rates, inset, Fig. 2(a). As shown in Fig. 2(c), the pull-off force increases with the unloading rate following an S-shaped growth curve. This increase in the pull-off force with the detachment rate can be thought of as an increase in the apparent work of adhesion with the rate of unloading. Using contact mechanics models and treating the two fibers as cylinders with individual radii R_1 and R_2 interacting in crossed configuration with effective radius $R = \sqrt{R_1 R_2}$, the pull-off force is related to the apparent work of adhesion, w' as:

$$P_{pull-off} = -\psi \pi R w' \tag{1}$$

For the two extreme cases of adhesive contact and force control conditions, ψ lies between 1.5 (JRK model which is valid for soft adhering solids with large elastic deformation) (Johnson et al., 1971) and 2 (DMT model which is valid for hard solids with negligible elastic deformation) (Derjaguin et al., 1975). The JKR and DMT models for elastic contact are distinguished by the two extreme values of the non-dimensional Tabor parameter, $\mu = (Rw^2/(E^*2z_0^3))^{1/3}$. The reduced elastic modulus $E^* = [(1-\nu_1^2)/E_1 + (1-\nu_2^2)/E_2]^{-1}$ with E_1 , ν_1 , E_2 , and ν_2 being the elastic moduli and Poisson's ratios of materials 1 and 2 forming the contact; z_0 is the equilibrium distance between the two surfaces in contact; and w is the work of adhesion, which is the work required to separate two elastic bodies in contact. For intermediate values of μ , Maugis (1992) provided a closed form solution using the Dugdale approximation, where the adhesive stress σ_0 assumes a constant value until a critical separation, h_0 , between the two surfaces is reached and the force interaction vanishes.

It has been shown (Das and Chasiotis, 2020) that the work of adhesion of PAN nanofibers at the extremely slow detachment rate of 12 nms^{-1} is $101 \pm 11 \text{ mJ/m}^2$ or $96 \pm 11 \text{ mJ/m}^2$, calculated by using the JKR or the M-D elastic contact model, respectively, which is twice the surface energy of bulk PAN (Li et al., 2001). These literature results are consistent with the experimental results in Fig. 2(c): For instance, at the slowest unloading rate, the work of adhesion w= $-P_{\text{pull-off}}/(1.5\pi R)$ (assuming the JKR model is valid) is calculated as 102 mJ/m^2 ($P_{\text{pull-off}}$ =-91 nN) and 106 mJ/m^2 ($P_{\text{pull-off}}$ = $-1.02 \,\mu\text{N}$), for fibers with 380-nm and 4100-nm diameter, respectively. These values for the work of adhesion are within one-standard deviation from the values reported in (Das and Chasiotis, 2020). However, the aforementioned contact models must be revisited to account for the time-dependent effects demonstrated by the experiments in Fig. 2 (c). This objective is implemented in the next Sections in a linear elastic fracture mechanics (LEFM) framework to obtain an adhesion model that accounts for viscoelastic effects. As a background, we first review the elastic contact solution that has been shown to be valid at very slow detachment rates (12 nms $^{-1}$), and then expand our discussion to the viscoelastic contact solution. Furthermore, it has been shown (Das and Chasiotis, 2020) that, contrary to using z_0 =0.165 nm, a value z_0 =1 nm could predict the experimental pull-off instabilities during stick-slip sliding of two PAN nanofibers. Notably, the commonly used value of z_0 =0.165 nm was originally obtained for a closed packed solid (Israelachvili, 2015), and some prior contact studies with polymers have adopted a more realistic value of z_0 =1 nm (Shi et al., 2010; Wang et al., 2012; Stachewicz et al., 2014).

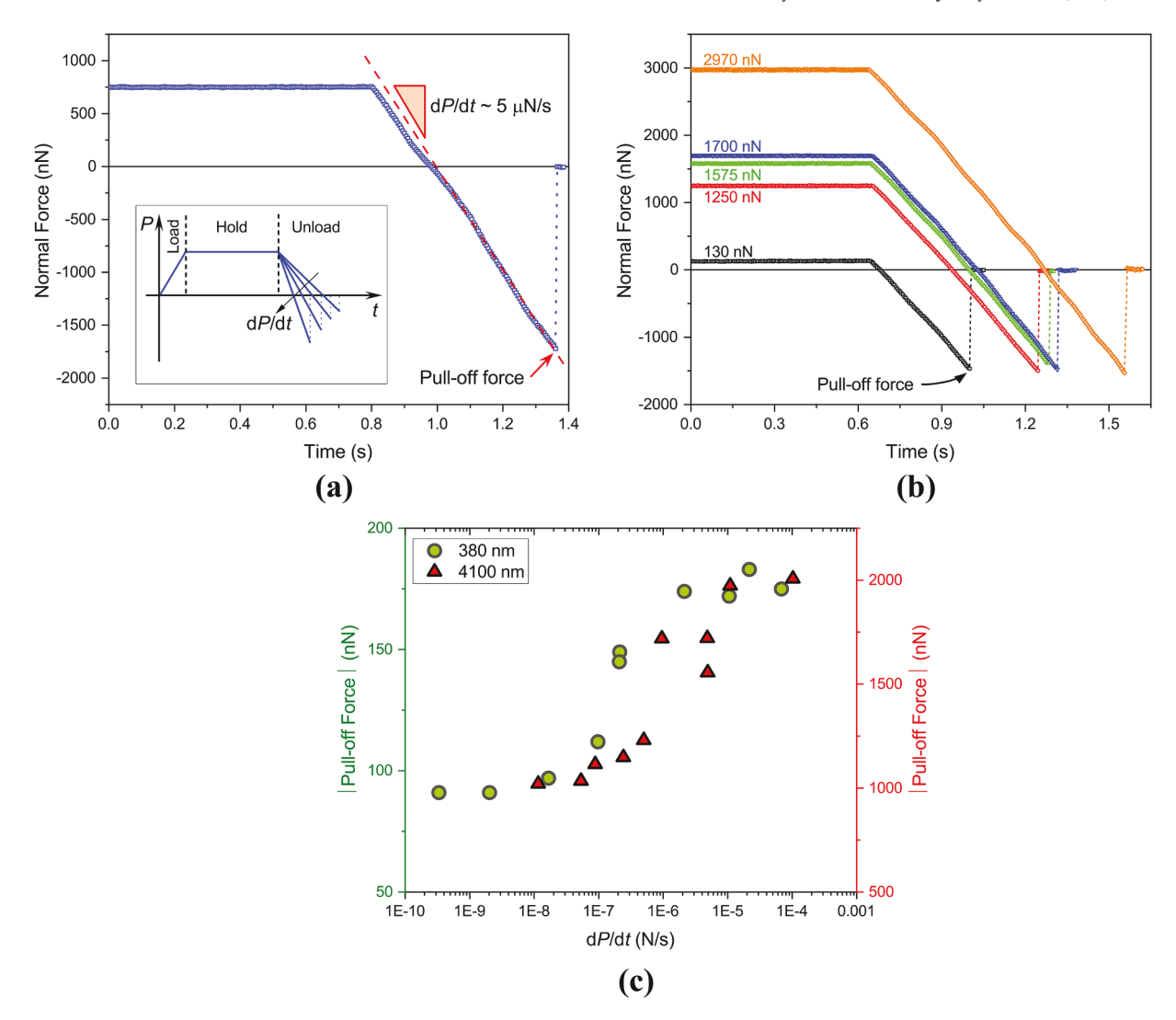


Fig. 2. (a) Force vs. time in a normal detachment experiment between two 4100 nm diameter fibers, showing the hold stage (flat portion) and the unloading stage. The inset shows a schematic of detachment tests with load, hold, and unloading stages. Note that with increase in unloading rate, the pull-off force increases. The loading rate was constant in all experiments and equal to 12 nms⁻¹ to minimize viscoelastic effects. (b) Force vs. time in a normal detachment experiment with different initial compressive preloads applied to the contact of two 3450 nm diameter fibers, showing that the preload does not influence the pull-off force. (c) Pull-off force vs. unloading rate for two fibers with diameters differing by one order of magnitude. (For interpretation of the references to color in this figure, the reader is referred to the web version of this article.)

3.2. Adhesive contact between elastic fibers

For a perfectly elastic material, energy flows from the far field to drive the creation of new crack surfaces, and the critical energy release rate, G_c , is equal to the work of adhesion. For $\mu \ge 5$, i.e., when the JKR elastic contact model and LEFM are valid (Das and Chasiotis, 2020), the adhesive force, P_a , gives rise to a singular tensile stress at the contact periphery. As a result, the mode I stress intensity factor, K_I , is related to the energy release rate, G_c , and the contact radius, G_c , as (Waters and Guduru, 2010; Papangelo and Ciavarella, 2019):

$$G = \frac{K_I^2}{2E^*} = \frac{P_a^2}{8\pi E^* a^3} \tag{2}$$

Crack initiation occurs when $G = G_c$ which is equal to the work of adhesion, w. This gives:

¹ LEFM is valid when the process zone is very small compared to other problem dimensions. It can be shown that for $\mu \ge 5$, the ratio of the cohesive zone size to the contact radius, d/a << 1, and, thus, the LEFM conditions are met.

$$G = G_c = w \Rightarrow P_a = \sqrt{8\pi E^* a^3 w} \tag{3}$$

The JKR relation between the applied normal force, P, and contact radius, a, for two elastic cylinders with equivalent radius R is given by:

$$P = P_H - P_a = \frac{4E^* a^3}{3R} - \sqrt{8\pi E^* a^3 w}$$
 (4)

where P_H is the equivalent Hertzian contact force that results in contact radius a in the absence of adhesion. Eq. (4) obeys the contact mechanics sign convention in which compressive forces are considered positive, and can be written in normalized form as:

$$\overline{P} = \overline{a}^3 - \sqrt{6\overline{a}^3} \tag{5a}$$

$$\overline{P} = \frac{P}{\pi R w}$$
 and $\overline{a} = a \left(\frac{4E^*}{3\pi w R^2}\right)^{1/3}$ (5b)

Herein, both test fiber segments were obtained from the same long fiber, $R_1 = R_2 = R$, which, for a normal cross-cylinder configuration, results in circular contact area.

The JKR elastic contact model is conceptually equivalent to the small-scale yielding (SSY) approximation in LEFM. The region where adhesion forces act is small compared to the contact radius, which is equivalent to the dimensions of the process zone compared to the crack length (or any other dimensions) in the SSY approximation. In the JKR model, the adhesive tensile stress is infinite at the edge of the contact and thus, for a growing crack, the material near the crack tip experiences an "infinite" loading rate (Hui et al., 1998). The material response to this infinite rate of loading depends only on the instantaneous elastic response, and, therefore, interface crack propagation and growth in the JKR model do not depend on the crack tip velocity. However, this is not what is observed in Fig. 2(c). A similar well-known paradox in viscoelastic fracture mechanics was resolved by Schapery (1975) and Knauss (1970) by using a non-zero cohesive zone length, analogous to the M-D elastic contact model (Maugis, 1992). This cohesive zone renders the stresses finite everywhere, and, as a result, the material response does not depend on the instantaneous elastic properties, hence giving rise to rate-dependent crack growth.

Compared to the JKR model, the M-D model provides a more versatile treatment of the elastic contact adhesion problem for a wide range of values for μ . In the M-D model, a cohesive zone exists outside the intimate contact region of radius a, which eliminates the stress singularity in the JKR model. The cohesive zone with a constant adhesive tensile stress, σ_0 extends to a radius c (m=c/a), while in the annulus a < r < c, the surface separation increases monotonically from zero to a value h_0 , beyond which the two surfaces no longer interact with each other. The work of adhesion is then equal to $w = \sigma_0 h_0$. The value of the critical separation is obtained by energy balance as $h_0 = (9\sqrt{3}/16)z_0 \approx 0.97z_0$ and satisfies the condition that the work of adhesion, w, with a force per unit area, σ_0 , is equal to the interaction energy due to the Lennard-Jones potential in the adhesion region. The Maugis parameter, λ , in the M-D model, which is equivalent to Tabor's parameter ($\lambda = 1.16\mu$), determines the strength of the adhesive tensile stresses and the extent of the cohesive zone. As λ increases from zero to infinity, there is a continuous transition from the DMT model to the JKR model. As a rule of thumb, the DMT model is valid for μ (or λ) < 0.1, while the JKR model is valid for μ (or λ) > 5. In the M-D model, the following two equations are solved simultaneously to relate \overline{P} and \overline{a} :

$$\frac{1}{2}\lambda \overline{a}^{2} \left\{ (m^{2} - 2)\cos^{-1}(1/m) + \sqrt{m^{2} - 1} \right\} + \frac{4}{3}\overline{a}\lambda^{2} \left\{ \sqrt{m^{2} - 1}\cos^{-1}(1/m) - m + 1 \right\} = 1, \tag{6a}$$

$$\overline{P} = \overline{a}^3 - \lambda \overline{a}^2 \left\{ m^2 \cos^{-1}(1/m) + \sqrt{m^2 - 1} \right\}$$
(6b)

The first term in Eq. (6b), is the Hertzian contact component, as in Eq. (5a), and the second term is the adhesive component which depends on λ and m. For large λ , $(c-a)/a = (m-1) \rightarrow 0$ and Eq. (6b) reduces to Eq. (5a), i.e., the JKR case.

3.3. Adhesive contact of viscoelastic fibers

The aforementioned adhesive contact models were extended in the past to account for the linear viscoelastic response of two cylinders in contact. The analogy between a moving crack in a viscoelastic solid and the kinetics of an adhering interface can be understood by considering a system of two semi-infinite solids with an interface crack and a M-D adhesive traction distribution (Johnson, 1999). The crack propagates under equilibrium conditions at a steady velocity V, by sliding a frictionless pin at the crack mouth. For a perfectly elastic solid, if the pin moves towards the crack tip, the work done by sliding the pin exactly balances the work done against the surface forces, w, (Eq. (3)) since the stored elastic strain energy does not change by displacing the pin. Similarly, the same holds when the crack heals as the pin moves away from the crack tip. For a viscoelastic material, on the other hand, there is energy dissipation as the strain field moves through the material, and the process of crack opening is different from that of crack healing. Herein, the detachment problem is analogous to the process of crack opening. It is assumed that during crack opening in a viscoelastic material, a fraction f(V) of the available elastic energy G is dissipated, and therefore, from energy considerations (Johnson, 1999):

$$(G - f(V)G) = G_c = w \tag{7a}$$

$$\frac{G}{w} = \frac{1}{(1 - f(V))} = \chi(V) \ge 1 \tag{7b}$$

According to (Johnson, 1999), for an opening crack, the fraction of dissipated energy, f, increases with local crack tip velocity V. Eq. (7b) can also be written as: G = w/(1-f), which is interpreted as follows: in a viscoelastic material, a crack initiates when the available elastic energy becomes equal to the modified critical energy release rate, w' = w/(1-f). Thus, the apparent work of adhesion, w', is greater than the extremely slow-rate (elastic) work of adhesion, w, since $0 \le f < 1$. It also follows that the function $\chi(V)$ is required to determine w'. Schapery (1975) investigated the mechanics of crack initiation in viscoelastic materials, which was used by Johnson and Greenwood to show that for an opening crack (Johnson, 1999; Greenwood and Johnson, 2006):

$$\chi(V) \cong \frac{1}{j(t^*)} \tag{8}$$

where $j(t^*)$ is the normalized creep compliance function of the viscoelastic material at a representative time t^* , which is the time needed for the crack tip moving with velocity V to traverse a length d^* of the effective process zone, namely $d^*=Vt^*$.

In the present study, the PAN fibers are assumed to behave in a linearly viscoelastic manner (also supported by the works of Naraghi et al. (2014), and Shrestha et al. (2020)) which makes the problem mathematically tractable. Furthermore, a simple 3-element standard linear solid (comprised of two springs and one dashpot) model is used to describe the small strain deformation behavior (Johnson, 1999; Greenwood and Johnson, 2006). At extremely low and high deformation rates, the standard linear solid behaves elastically with moduli, E_{∞}^* and E_0^* , known, respectively, as the relaxed and the instantaneous moduli. At intermediate rates, the strain $\varepsilon(t^*)$ at a representative time t^* for a step change in stress σ is given by $\varepsilon(t^*) = J(t^*)\sigma$, where $J(t^*)$ is the creep compliance function:

$$J(t^*) = \frac{1}{E_{\infty}^*} \left[1 - \left(1 - \frac{E_{\infty}^*}{E_0^*} \right) \exp\left(-\frac{t^*}{\tau} \right) \right] = \frac{1}{E_{\infty}^*} j(t^*)$$
 (9a)

$$j(t^*) = \left[1 - (1 - k)\exp\left(-\frac{t^*}{\tau}\right)\right]; \quad k = \frac{E_{\infty}^*}{E_0^*},$$
 (9b)

where, τ is the viscoelastic time constant of the material, and k is the ratio of the relaxed modulus to the instantaneous modulus.

It is apparent that the Hertzian and the adhesive contributions in both the JKR and the M-D elastic contact models, Eqs. (5a) and (6b), have different length scales associated with them. There is the bulk deformation of the contact arising principally from the Hertzian contact force P_H , whose size is characterized by the radius a of the contact. The characteristic time for this bulk deformation is $t_0 \sim a_0/V$, where a_0 is the contact radius at the maximum compressive force. There is also a strain concentration just outside the intimate contact region produced by adhesive forces, whose size is characterized by the effective length d^* of the Dugdale zone, and thus, the characteristic time associated with the adhesive force P_a is $t^* \sim d^*/V$. Using Schapery's arguments, Greenwood and Johnson (2006) showed that for an opening crack, the effective process zone length can be considered as $d^* \sim d_0/3$, where d_0 is the cohesive zone length (c-a) in the M-D model. Hence, the ratio of the characteristic times governing the strain rate in the two locations (Greenwood and Johnson, 2006) is $t^*/t_0 \sim d^*/a_0 < 1$ for $\lambda \ge 1$ (when the length of the effective process zone is small compared to the initial contact radius). For reference, the maximum value of $d^*/a \sim 0.2$ for $\lambda = 1$, with a being the contact area at pull-off. This means that the viscoelastic effect at the edge of the contact due to the adhesive force P_a can be separated from that in the Hertzian contact due to the force P_H . Thus, the Hertzian contact deformation can be assumed to be relatively very slow, elastic, and reversible with relaxed modulus, E_∞^* , whereas all viscoelastic effects are confined to the adhesion term in Eq. (4). It should be noted, that the current study only considers the viscoelastic effects of the polymer and does not delve into the rate dependence of the adhesive interaction in the cohesive zone itself, as reported for example in Liechti and Wu (2001).

3.4. Extended JKR model for viscoelastic contact

The extension of the elastic JKR solution to account for viscoelastic effects is briefly reviewed here for completeness. In this problem formulation, the total normal force in a viscoelastic adhesive contact can be written as (Greenwood and Johnson, 2006):

$$P = P_H - P_a = \frac{4E_{\infty}^* a^3}{3R} - \sqrt{8\pi(\chi w)E_{\infty}^* a^3} \Rightarrow \overline{P} = \overline{a}^3 - \sqrt{6\overline{a}^3\chi}, \tag{10a}$$

$$\overline{P} = \frac{P}{\pi R w}$$
 and $\overline{a} = a \left(\frac{4E_{\infty}^*}{3\pi w R^2} \right)^{1/3}$ (10b)

where the work of adhesion is replaced by the apparent work of adhesion, χw (Eq. (7)), while the Hertzian contact contribution is considered elastic and reversible with relaxed modulus E_{∞}^* .

The relation between two experimentally measured quantities: the pull-off force and the rate of unloading, dP/dt, is required to utilize the extended JKR model for a viscoelastic material. Taking the derivative of \overline{P} w.r.t \overline{a} :

$$\frac{d\overline{P}}{d\overline{a}} = 3\left(\overline{a}^2 - \sqrt{\frac{3}{2}}\overline{a}\chi\right) - \sqrt{\frac{3}{2}}\frac{\overline{a}^3}{\chi}\frac{d\chi}{d\overline{a}}$$
(11)

The left-hand side in Eq. (11) can also be written as:

$$\frac{d\overline{P}}{d\overline{a}} = \left(\frac{d\overline{P}}{dt} \middle/ \frac{d\overline{a}}{dt}\right) = \left(\frac{\overline{P}/P}{\overline{a}/a}\right) \left(\frac{1}{V}\right) \frac{dP}{dt} \tag{12}$$

where the crack tip velocity is V = da/dt.

Equating (11) and (12), it follows that:

$$3\left(\overline{a}^2 - \sqrt{\frac{3}{2}}\overline{a}\chi\right) - \sqrt{\frac{3}{2}}\frac{\overline{a}^3}{\chi}\frac{d\chi}{d\overline{a}} = \left(\frac{\overline{P}/P}{\overline{a}/a}\right)\left(\frac{1}{V}\right)\frac{dP}{dt} = \left(\frac{3}{4\pi^2w^2RE_{\infty}^*}\right)^{1/3}\left(\frac{1}{V}\right)\frac{dP}{dt}$$

$$\tag{13}$$

If a relationship between the local crack tip velocity V and the parameter χ is obtained, then \overline{a} can be related to χ via the second equality in Eq. (13). Note that dP/dt is known from the experimental data. As described before, the crack tip velocity V is the ratio of the length of the effective process zone, d^* to the time taken to by the crack to traverse this distance:

$$V = \frac{d^*}{t^*} \approx \frac{d_0}{3t^*} \tag{14a}$$

$$d_0 \cong \frac{\pi E^* h_0^2}{4w} \Rightarrow d_0 \sim \frac{\pi}{4} \left(\frac{E_{\infty}^*}{j(t^*)} \right) \frac{h_0^2}{w},\tag{14b}$$

where d_0 =(c-a) in the first expression of Eq. (14b) was derived by Johnson, (1999) and Johnson and Greenwood (2002).

The JKR model does not have a cohesive zone length since (c-a)=0. However, an extended viscoelastic JKR model would require a cohesive zone length as explained in the previous Section. Towards this goal, Greenwood and Johnson (1981) used an argument from Israelachvili and Tabor (1972), supporting an inverse cube variation of the attractive forces between two surfaces, to obtain a rough estimate of the cohesive zone length as the distance (or separation) at which the attractive force falls to one eighth of its maximum value. The first expression in Eqn. (14b) gives an estimate of the cohesive zone size for an elastic material Johnson, 1999; Johnson and Greenwood, 2002), whereas for a viscoelastic material such an estimate is given by the second expression in Eq. (14b) (Greenwood and Johnson, 2006). Using Eqs. (9) and (14) the following relation between the crack tip velocity V and the parameter χ is obtained:

$$\left(\frac{t^*}{\tau}\right) \left[1 - (1-k)\exp\left(-\frac{t^*}{\tau}\right)\right] = \frac{\pi}{12} \frac{E_{\infty}^* h_0^2}{wV\tau}$$
 (15a)

which, with the aid of Eqs. (8, 9b), can be written as:

$$\frac{V}{\frac{\pi}{12} \left(\frac{\mathcal{E}_{\infty}^{L} h_0^2}{w\tau}\right)} = \frac{\chi}{\ln\left(\frac{1-k}{1-1/\chi}\right)}.$$
 (15b)

Finally, the ordinary differential Eq. (13) can be solved numerically by using an initial condition ($\overline{a} = \overline{a}_0$ for $\chi = 1$) to derive the relation between \overline{a} and χ . Once the relation between \overline{a} and χ has been obtained for a given value of dP/dt, a relation between \overline{P} and \overline{a} can then be derived through Eq. (10a), and the pull-off force for the same unloading rate dP/dt can be obtained by using the condition $d\overline{P}/d\overline{a} = 0$.

3.4.1. Extended DMT model for viscoelastic contact

The assumption that all viscoelastic effects are confined to the adhesion term breaks down when the length scales (and hence the time scales) associated with the adhesive contribution, i.e. the cohesive zone length, grow in comparison to the length (and time) scales associated with the Hertzian contribution. At the theoretical DMT limit, the size of the cohesive zone becomes infinite compared to the intimate contact region, and as such, the introduction of a "velocity-dependent adhesive energy" in the DMT limit appears inappropriate. However, Barthel and Roux (2000) used such an approach to obtain a relationship between the load and the intimate contact radius in the DMT limit as:

$$P = \frac{4E_{\infty}^* a^3}{3R} - 2\pi R(\chi w) \Rightarrow \overline{P} = \overline{a}^3 - 2\chi \tag{16}$$

The validity of Eq. (16) was established by Barthel and Roux (2000) via the argument that the same expression could also be derived through a self-consistent description of the contact between two elastic adhesive bodies in terms of the stress distribution outside the contact zone (Barthel, 1998), which allows for the introduction of nonequilibrium effects.

3.5. Extended M-D model for viscoelastic contact

In this research, the viscoelastic contact problem is approached from the perspective of the more general M-D model. The M-D model directly provides the cohesive zone size in contrast to the JKR model where there is no inherent cohesive zone and assumptions about the force-distance relations must be incorporated to estimate a cohesive zone length. In this work, the classic elastic M-D model is extended to a more general viscoelastic M-D model:

$$\frac{1}{2}\lambda_{\infty}\overline{a}^{2}\left\{\left(m^{2}-2\right)\cos^{-1}(1/m)+\sqrt{m^{2}-1}\right\}+\frac{4}{3}\overline{a}\lambda_{\infty}^{2}\left\{\sqrt{m^{2}-1}\cos^{-1}(1/m)-m+1\right\}=\chi,\tag{17a}$$

$$\overline{P} = \overline{a}^3 - \lambda_{\infty} \overline{a}^2 \left\{ m^2 \cos^{-1}(1/m) + \sqrt{m^2 - 1} \right\}$$
(17b)

where the normalized force and contact radius are given by Eq. (10b). The Maugis parameter, λ_{∞} has been computed using the relaxed modulus of the polymer. The model assumes that the time scale associated with the bulk deformation of the contact (arising from the Hertzian contact force) is sufficiently long and, therefore, the deformation is still elastic, with the modulus being close to the relaxed modulus of the polymer. All viscoelastic effects are confined to the adhesion term.

Numerical calculations were carried out by using Eqs. (17a) and (17b) for both z_0 =0.165 nm and z_0 =1 nm. The work of adhesion, w was taken as 100 mJ/m². If z_0 =0.165 nm is assumed, then λ_∞ =6 (400 nm fiber diameter) and λ_∞ =14 (4000 nm fiber diameter), and thus, the M-D model is closer to the extended JKR model discussed in Section 3.4. However, if z_0 =1 nm is assumed, which was shown to provide better agreement with experiments on adhesive sliding of polymer nanofibers (Das and Chasiotis, 2020), then λ_∞ =1 (400 nm diameter) and λ_∞ =2 (4000 nm diameter), which means that the extended viscoelastic JKR model discussed in the previous Section is no longer valid and the extended M-D model must be employed.

3.5.1. Extended M-D model for viscoelastic contact: z_0 =0.165 nm

Using the elastic M-D model, Eq. (6), it can be shown, Fig. 3(a), that the length of the cohesive zone (at extremely slow peeling velocities) is roughly proportional to the reduced elastic modulus, $d_0 \propto E^*$. Increasing values of E^* decrease both radii a and c, as deduced from Fig. 3(b) for 400 nm fiber diameter. However, $d_0 = (c-a)$ increases due to the decrease in the value of λ with increasing E^* , which pushes the contact towards the DMT approximation. The cohesive zone length found numerically for a given value of λ , depends on the applied normal force. Fig. 3(a) shows that the analytical expression represented by the dashed line (Eq. (14b)) captures well the variation of the cohesive zone length with E^* for large fiber diameters (4000 nm) but not so well for smaller fiber diameters (400 nm). Furthermore, the inset in Fig. 3(a) shows that the conditions for LEFM are met when $\lambda \ge 5$ ($z_0 = 0.165$ nm) since the ratio of the non-linear cohesive zone to the contact radius is $(c-a)/a \ll 1$. For instance, for the case $E^* = E_0^*$, (c-a)/a is ~ 0.04 and ~ 0.01 for 400 nm and 4000 nm fiber diameter, respectively.

The value of χ is required to apply the extended viscoelastic M-D model, Eq. (17). χ can be obtained from $j(t^*)$, Eq. (8), but the value

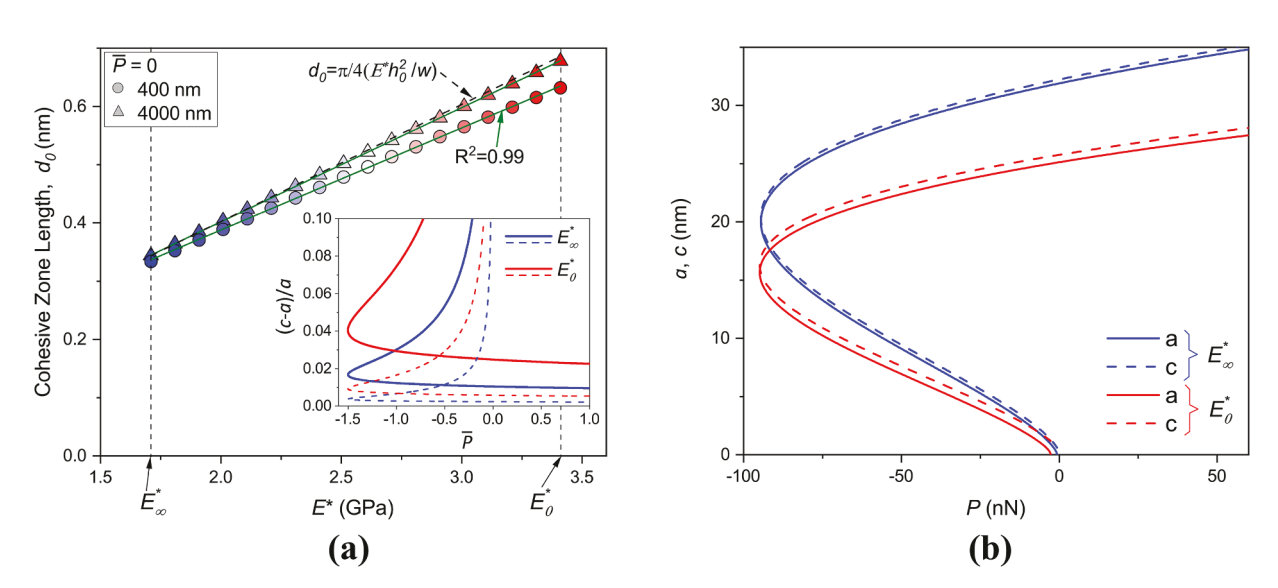


Fig. 3. (a) Cohesive zone length (at P=0 for extremely slow peeling velocities) obtained using the elastic M-D model for z_0 =0.165 nm. Note that for z_0 =0.165 nm and for both 400 nm and 4000 nm fiber diameters, one finds λ >5. The cohesive zone length is proportional to the reduced elastic modulus and its variation for the 4000 nm fiber is captured well by the analytical expression given by Greenwood and Johnson: $d_0 = \pi E^* h_0^2 / (4w)$ (Johnson, 1999). The inset shows the ratio of the cohesive zone length over the contact radius for z_0 =0.165 nm and fiber diameters 400 nm (solid lines), 4000 nm (dashed lines). The non-linear cohesive zone is much smaller than the contact radius. (b) The cohesive zone length increases with increasing E^* due to the decrease in the value of λ , which pushes the contact towards the DMT regime. A fiber with 400 nm diameter was assumed for the calculations in this plot. (For interpretation of the references to color in this figure, the reader is referred to the web version of this article.)

of k is then needed to calculate j, Eq. (9b). The value of $k = E_{\infty}^*/E_0^*$ was obtained from Naraghi et al. (2014), where uniaxial tension tests were performed on PAN nanofibers as a function of strain rate. For a fiber with 300 nm diameter, the ratio of the tangent modulus measured at $2.5 \times 10^{-4} \, \mathrm{s}^{-1}$, to the modulus obtained at $2 \times 10^2 \, \mathrm{s}^{-1}$, provided $k = E_{\infty}^*/E_0^* = 0.5$. In this study k is considered to be independent of the fiber diameter, since the electrospun PAN fibers were annealed, and therefore their elastic properties are not expected to be size dependent for the particular range of diameters, as also reported in Das and Chasiotis (2020). Finally, the values $E_{\infty}^* = 3$ GPa (Das and Chasiotis, 2020) and $E_0^* = 6$ GPa are used in all subsequent calculations. For k = 0.5, the values of j and χ are in the range: $0.5 \le j(t^*) \le 1$ (Eq. (9b)) and $1 \le \chi \le 2$ (Eq. (8)). Based on these bounds, the solution of Eq. (17) is plotted in Fig. 4(a) for the extreme values of χ (red and blue curves: $\chi = 1$; black and gray curves: $\chi = 2$), and for two relatively extreme values of λ_{∞} . Furthermore, the extended JKR solution, for the extreme values of the parameter λ_{∞} .

For a viscoelastic material and a given unloading rate dP/dt, Eq. (17) must be solved for the $\overline{a} - \overline{P}$ relation. However, in Eq. (17a,b) the force and the contact radius are not related one-to-one as in Eq. (10a). Therefore, a graphical approach was adopted to obtain $d\overline{P}$

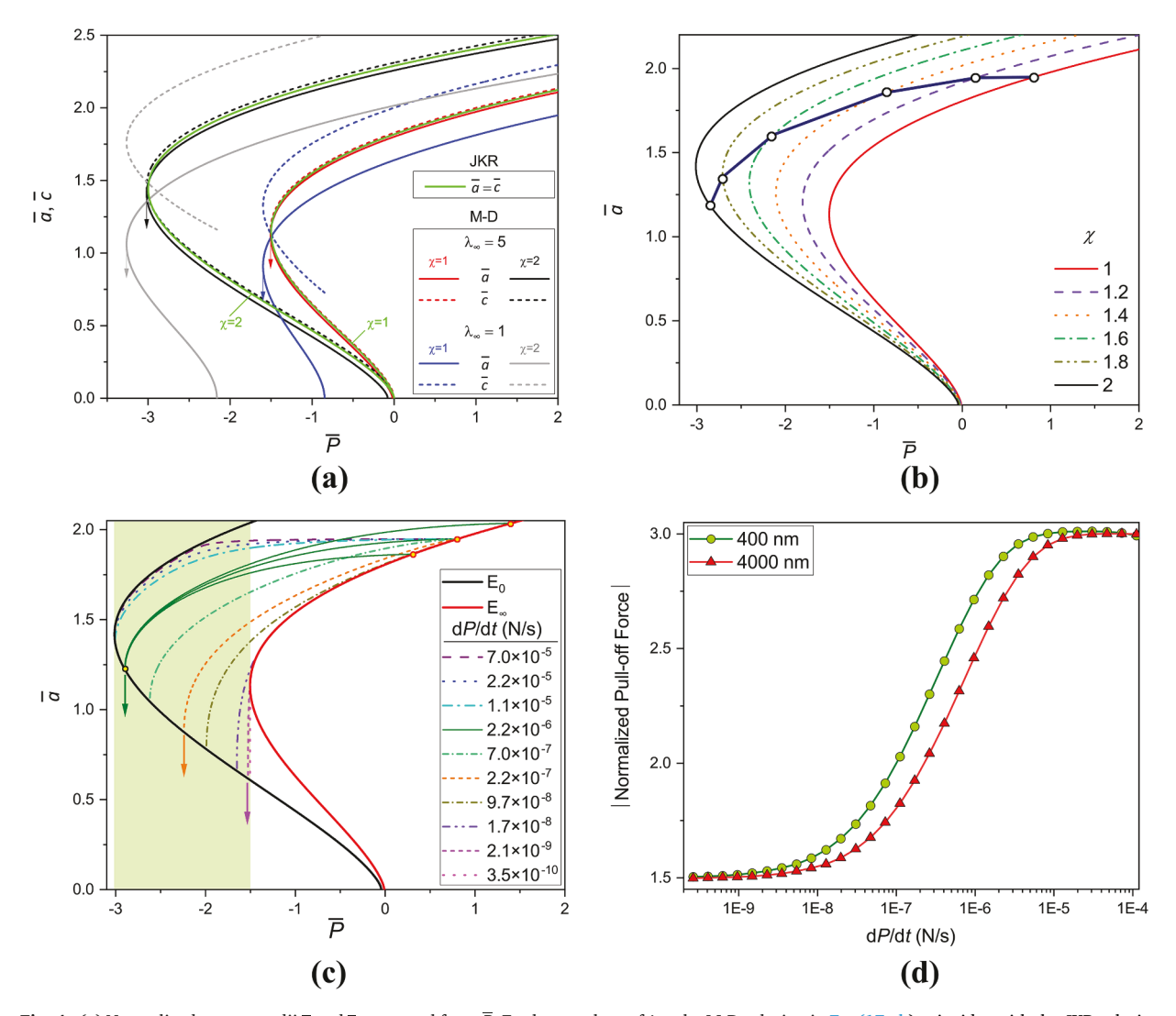


Fig. 4. (a) Normalized contact radii \bar{a} and \bar{c} vs normal force \bar{P} . For large values of λ_{∞} , the M-D solution in Eq. (17a,b) coincides with the JKR solution in Eq. (10a), for the extreme values of χ . The points leading to the force-controlled snap-off instability are represented by the arrows. (b) Graphical method to obtain the $\bar{a} - \bar{P}$ solution following the extended M-D model ($dP/dt = 10^{-6}$ N/s). (c) Simulated $\bar{a} - \bar{P}$ for various unloading rates of a viscoelastic PAN fiber with diameter 400 nm and $\tau = 5$ ms. The pull-off force, indicated by the arrows, increases with unloading rate. The three different values of the initial contact radius in the compression region, represented by the three yellow points on the red curve, result in the same pull-off force for the same unloading rate of 2.2×10^{-6} N/s, namely the initial preload does not influence the pull-off force. (d) Simulated normalized pull-off force vs. unloading rate for $\tau = 5$ ms. (For interpretation of the references to color in this figure legend, the reader is referred to the web version of this article.).

 $/d\overline{a}$. As shown in Fig. 4(b), $\overline{a} - \overline{P}$ curves were constructed for various values of the parameter χ by using Eq. (17a,b). The initial condition $\overline{a} = 1.9$ for $\chi = 1$ was used to obtain the first point. Choosing other values for the initial contact radius (in the hold stage when the contact is in compression) did not change the calculated pull-off force. An unloading rate $dP/dt = 10^{-6}$ N/s and $\tau = 5$ ms were chosen to demonstrate the solution procedure. The cohesive zone length, d_0 (for the first point, $\overline{a} = 1.9$, $\chi = 1$) can be obtained numerically from Eq. (17) as: $(\overline{c} - \overline{a})$. The cohesive zone length can then be used to calculate the crack velocity V according to Eq. (14a). The value of t^* is obtained by inverting Eq. (9b) (χ provides the value of f, Eq. (8)). The right-hand side of Eq. (13) (or Eq. (12)) can be obtained for known values of $[V, dP/dt, R, w, E_{\infty}^*]$, which is also equal to the slope $d\overline{P}/d\overline{a}$. Knowing the first point and the slope of the line, $d\overline{P}/d\overline{a}$, a straight line is drawn that intersects the $\overline{a} - \overline{P}$ curve constructed for $\chi = 1.2$. Again, the new value of χ and the cohesive zone size, $(\overline{c} - \overline{a})$, at the point of intersection provide the crack velocity and hence the slope of the next line at the point of intersection. Proceeding similarly, the entire $\overline{a} - \overline{P}$ curve for a particular unloading rate, shown with five straight segments in Fig. 4(b), can be constructed.

Following the approach described in Fig. 4(b), the $\overline{a} - \overline{P}$ curves were constructed for very small increments of the parameter χ , leading to smooth $\overline{a} - \overline{P}$ curves for different values of dP/dt that are shown in Fig. 4(c). The resulting smooth curves intersect the solid black curve at steep angles $(da/dP \rightarrow \infty)$, leading to snap-off instabilities and providing the pull-off forces. This is due to the fact that $(1/V) \rightarrow 0$ as $\chi \rightarrow (1/k) = 2$ (Greenwood and Johnson, 2006; Johnson, 1999), leading to $dP/da \rightarrow 0$ (Eq. 12). The pull-off force, indicated by the arrows in Fig. 4(c), increases with dP/dt, following the *S*-shaped growth curves in Fig. 4(d). Furthermore, choosing other values for the initial contact radius (e.g. just before unloading when the contact is in compression) does not change the results: for instance, three different values of the initial contact radius in the compression region produce the same pull-off force for the unloading rate of 2.2×10^{-6} N/s, Fig. 4(c). This also implies that, the initial preload does not influence the pull-off force, as was also demonstrated experimentally in Fig. 2(b). Other numerical studies have also shown that the pull-off force is independent of (a) the initial contact radius for a wide range of velocities and dissipation exponents (Barthel and Roux, 2000), and (b) the initial compressive preload (Greenwood and Johnson, 2006) for a wide range of unloading rates.

It should be noted that the pull-off force was calculated at the pull-off instability for a force-controlled experiment by using the condition dP/da=0. The experiments in this work were conducted by imposing constant crosshead velocities. However, the experimental system, comprised of two MEMS force sensors and two polymer fibers, has a finite stiffness due to the finite spring constant of the MEMS folded beam load cells and the finite bending stiffness of the fibers in contact that are functioning as springs in series with the MEMS devices. These experimental parameters lead to a compliant system: as the fiber surfaces in contact are displaced away from each other at a prescribed crosshead velocity, it is not the applied displacement but the force that arises which controls the evolution of the contact. The pull-off instability in a force-controlled experiment occurs when the condition $dP/da\rightarrow 0$ (or $dP/d\delta\rightarrow 0$, with δ being the displacement) is met.

Finally, the computed pull-off force as a function of the unloading rate follows an S-shaped growth curve that is shifted to the right for increasing fiber diameter, Fig. 4(d), which is in agreement with the experimental results in Fig. 2(c). This shift originates in the prefactor $(\overline{P}/P)/(\overline{a}/a)$ in Eq. (13), which depends on the fiber diameter. The results in this Section were based on the general assumption that z_0 =0.165 nm, which has been derived for close packed solids (Israelachvili, 2015). However, as shown by Das and Chasiotis (2020), a value of z_0 =1 nm provides better agreement with the experimental results for the pull-off instability during shear detachment of polymer nanofibers. The next Section explores the use of z_0 =1 nm which, in turn, results in $1 < \lambda_{\infty} < 5$, and, therefore, the extended M-D model must be used to describe the adhesive contact.

3.5.2. Extended M-D model for viscoelastic contact: z_0 =1 nm

The approach described in Section 3.5.1was also applied for the case of z_0 =1 nm, which was shown before to provide a better agreement with experimental tangential pull-off force values measured during adhesive sliding of PAN nanofibers (Das and Chasiotis, 2020). Also, when z_0 =1 nm, λ_∞ =1 (400 nm diameter) and λ_∞ =2 (4000 nm diameter), implying that the extended M-D model must be employed, as the extended JKR model, Section 3.4, is no longer valid. Fig. 5(a) shows simulated $\bar{a} - \bar{P}$ curves for various unloading rates of a viscoelastic PAN fiber with diameter 4000 nm and τ =50 ms. The normalized pull-off force, indicated by the arrows, increases with the unloading rate following *S*-shaped growth curves (as in Section 3.5.1), Fig. 5(b). Note that for the same value of the work of adhesion, w=100 mJ/m², the normalized pull-off force at the two unloading rate extremes increases with decreasing fiber diameter, Fig. 5(b). This is due to the decrease in the value of λ_∞ with decreasing fiber diameter which, in turn, increases the normalized pull-off force (Fig. 4(a) shows that the normalized pull-off force increases with decreasing λ_∞ for curves generated with the extreme values of χ). Equivalently, a gradual decrease in the fiber diameter, and consequently decrease in the value of λ_∞ , leads to an increase in the value of ψ , Eq. (1), from 1.5 to 2 as the contact model transitions from the JKR to the DMT model under force control.

Note that the extended M-D model developed in this study has the same inherent assumption as the extended JKR model in Section 3.4 in which the viscoelastic effects are confined to the adhesion term whereas the Hertzian contribution is relatively slow, elastic, and reversible. This is also reflected in Fig. 4(a) where the extended M-D model converges to the extended JKR model for $\lambda_{\infty} \ge 5$. As described in Section 3.3, the assumption that the Hertzian contribution is slow and elastic is appropriate only when the size of the initial contact radius is much larger than the cohesive zone length (see also the relevant discussion in Greenwood and Johnson (2006)). This limits the application of the extended M-D model to cases where $\lambda_{\infty} \ge 1$; when $\lambda_{\infty} = 1$, the maximum value of $d^*/a \sim 0.2$, with a being the contact radius at pull-off. The extended M-D model applied in this work can, thus, be considered as valid even for $\lambda_{\infty} = 1$, since the criterion by Greenwood and Johnson (2006), $d^*/a_0 < 1$ is still satisfied, where a_0 is the initial contact radius at the maximum compressive force.

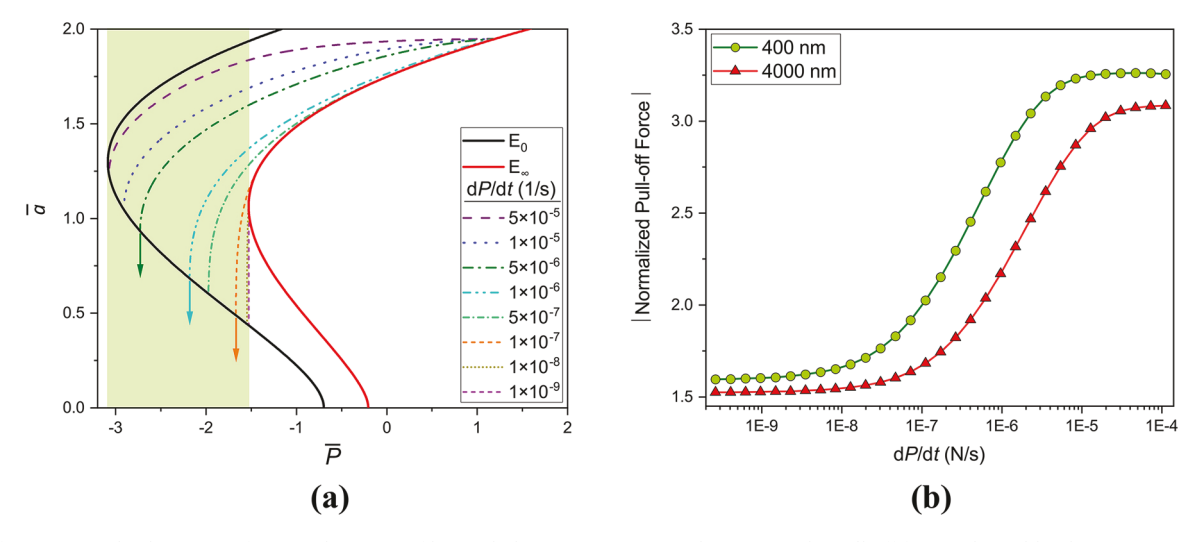


Fig. 5. (a) Simulated $\bar{a} - \bar{P}$ for various unloading rates of a viscoelastic PAN fiber with diameter 4000 nm and τ =50 ms. The pull-off force indicated by the arrows increases with unloading rate. (b) Simulated normalized pull-off force vs. unloading rate for τ =50 ms following *S*-shaped growth and a shift with fiber diameter, consistently with the experimental results in Fig. 2(c). (For interpretation of the references to color in this figure, the reader is referred to the web version of this article.)

3.6. Identification of viscoelastic time constants from normal detachment data

The normal pull-off force at the slowest unloading rate could be used to obtain the work of adhesion, w, for the fully elastic condition. Specifically, for the 380 nm fiber diameter, $w=101 \text{ mJ/m}^2$ ($z_0=0.165 \text{ nm}$) and $w=95 \text{ mJ/m}^2$ ($z_0=1 \text{ nm}$), and for the 4100 nm fiber diameter, $w=106 \text{ mJ/m}^2$ ($z_0=0.165 \text{ nm}$) and $w=103 \text{ mJ/m}^2$ ($z_0=1 \text{ nm}$). All values are within one standard deviation of the work of adhesion values obtained in a previous work on PAN nanofibers (Das and Chasiotis, 2020). Using the aforementioned values for w, the experimental pull-off force measurements are compared to theoretical predictions. Fig. 6(a) and (b) show the experimental and calculated normalized pull-off force vs. unloading rate for z_0 =0.165 nm and z_0 = 1 nm, respectively. There is good agreement between the experimental pull-off force values and the model predictions for relaxation time constants in the range of $\tau=2-6$ ms $(z_0=0.165 \text{ nm})$ and $\tau=45-90 \text{ ms}$ $(z_0=1 \text{ nm})$. These time-constants were obtained by maximizing the coefficient of determination, R^2 between experimental and numerical data. Numerical simulations were carried out with varying time-constants and 1 ms time-resolution to obtain the best fit value of τ , as described in Section 3.5.1. Note that the time constants obtained for z_0 =1 nm are more than one order of magnitude larger than those obtained for z_0 =0.165 nm. Mathematically speaking increasing z_0 , reduces the value of λ_{∞} which leads to an increase in the cohesive zone length. As a result, for a given fiber diameter and the same dP/dt, t^* increases proportionally to the cohesive zone length to maintain V, Eq. (14a) (and by extension the pull-off force), and, therefore, τ must also increase proportionally to t*, Eq. (9). As shown in Fig. 6(a,b), the smaller diameter fiber has larger time-constants, albeit of the same order of magnitude, than the thicker fiber, namely for a given unloading rate of the viscoelastic region, the normalized pull-off force is higher for the thinner fiber, Fig. 6(a,b). A similar increase in normalized pull-off force with decreasing fiber diameter was also obtained numerically using the same time constants for the thinner and the thicker fibers, Figs. 4(d) and 5(b), although the gaps between the red and green solid lines in Figs. 4(d) and 5(b) are narrower than those observed experimentally in Fig. 6(a,b). Increasing the time-constant shifts the red and green curves to the left (and vice-versa). As a result, the time-constants obtained from the best fit procedure are larger for the thinner fiber compared to the thicker fiber. The time constants are expected to be sensitive to the molecular orientation of the fiber surface (where contact takes place), which is influenced by the annealing step. Further studies are required to shed more light into the physical mechanisms influencing the time constants of different fiber diameters.

Although, it can be shown that there is a greater reduction in contact area during unloading for z_0 =1 nm (also observed during shear detachment experiments, see (Das and Chasiotis, 2020)), it cannot be asserted, however, which value of z_0 describes best the normal detachment process without direct observations of the contact area. For reference, prior creep and strain rate experiments were used to compute the viscoelastic time constants of PAN (Naraghi et al., 2014). The shortest time constant, computed from ramp data obtained at 200 s⁻¹, was ~15 ms, which is of the same order as the time constants extracted herein. These short time constants are relevant to local segmental relaxations at the fiber surface which are considered to be quite faster than molecular relaxations taking place in the fiber core. These fast time constants may also explain the fast recovery of PAN nanofiber surfaces which re-bond to the original strength right after each sliding jump instability in stick-slip experiments (Das and Chasiotis, 2020).

The estimated time constants for the contact problem could be used to evaluate the assumption for the shape and size of the contact before detachment. When two PAN nanofibers are brought in close proximity during a normal adhesion test, they snap-in and an initial contact area forms and grows with time to its equilibrium size (given by the contact radius for a particular normal force, as determined by the elastic JKR or M-D models). The time required to reach the equilibrium size might be 100 times larger than the viscoelastic time constant (Greenwood and Johnson, 2006). In the present experiments the fibers were held in contact and under compression for 15 min which is much longer than 100 times the extracted viscoelastic time constant. As a result, the initial contact size can be estimated by the elastic JKR or the M-D contact models. Moreover, the applied force remains stable during the initial hold stage, Fig. 1(a), which suggests that the contact radius does not increase after attaining equilibrium.

Finally, the dependence of the *S*-shaped curves on the Maugis (or Tabor) parameter is explored in Fig. 6(c). A normalized loading rate parameter, can be obtained if the cohesive zone length at pull-off (when $j(t^*)=0.5$) is considered to be a multiple, ϕ , of the theoretical value, Eq. (14b). Furthermore, a non-dimensional velocity, ν , (Johnson, 1999) can be defined as in Eq. (15b):

$$d_{pull-off} = \phi \frac{\pi}{4} \left(\frac{E_{\infty}^*}{j(t^*)}\right) \frac{h_0^2}{w} \tag{18a}$$

$$v \approx \frac{V}{\left(\phi \frac{\pi}{12} \frac{E_{\infty}^* h_0^2}{w\tau}\right)} = \frac{1}{\phi} \left(\frac{12wV\tau}{\pi E_{\infty}^* h_0^2}\right) \tag{18b}$$

Eq. (13) can be rewritten using the normalized velocity, which provides the normalized loading rate parameter, A (Johnson, 1999):

$$\frac{d\overline{P}}{d\overline{a}} = \left(\frac{3}{4\pi^2 w^2 R E_{\infty}^*}\right)^{1/3} \left(\frac{1}{V}\right) \frac{dP}{dt} = \frac{1}{\phi} \left(\frac{3}{4\pi^2 w^2 R E_{\infty}^*}\right)^{1/3} \left(\frac{12w\tau}{\pi E_{\infty}^* h_0^2}\right) \left(\frac{\pi R w}{v}\right) \frac{d\overline{P}}{dt}$$
(19a)

$$\Rightarrow \frac{d\overline{P}}{d\overline{a}} = \frac{d\overline{P}}{dt} \frac{\tau}{\phi} \left(\frac{36 Rw^2}{\pi E_{\infty}^{*2} h_0^3} \right)^{2/3} \left(\frac{1}{v} \right) = \frac{A}{v}; \qquad A = \frac{d\overline{P}}{dt} \frac{\tau}{\phi} \left(\frac{36 Rw^2}{\pi E_{\infty}^{*2} h_0^3} \right)^{2/3}$$
(19b)

Using the rate parameter *A* as the abscissa, the curves in Fig. 6(a,b) can be re-plotted using the time-constants obtained from the best-fitting procedure to show the dependence of the *S*-shaped curves on λ_{∞} . The value of ϕ is obtained from Eq. (18a) using the value

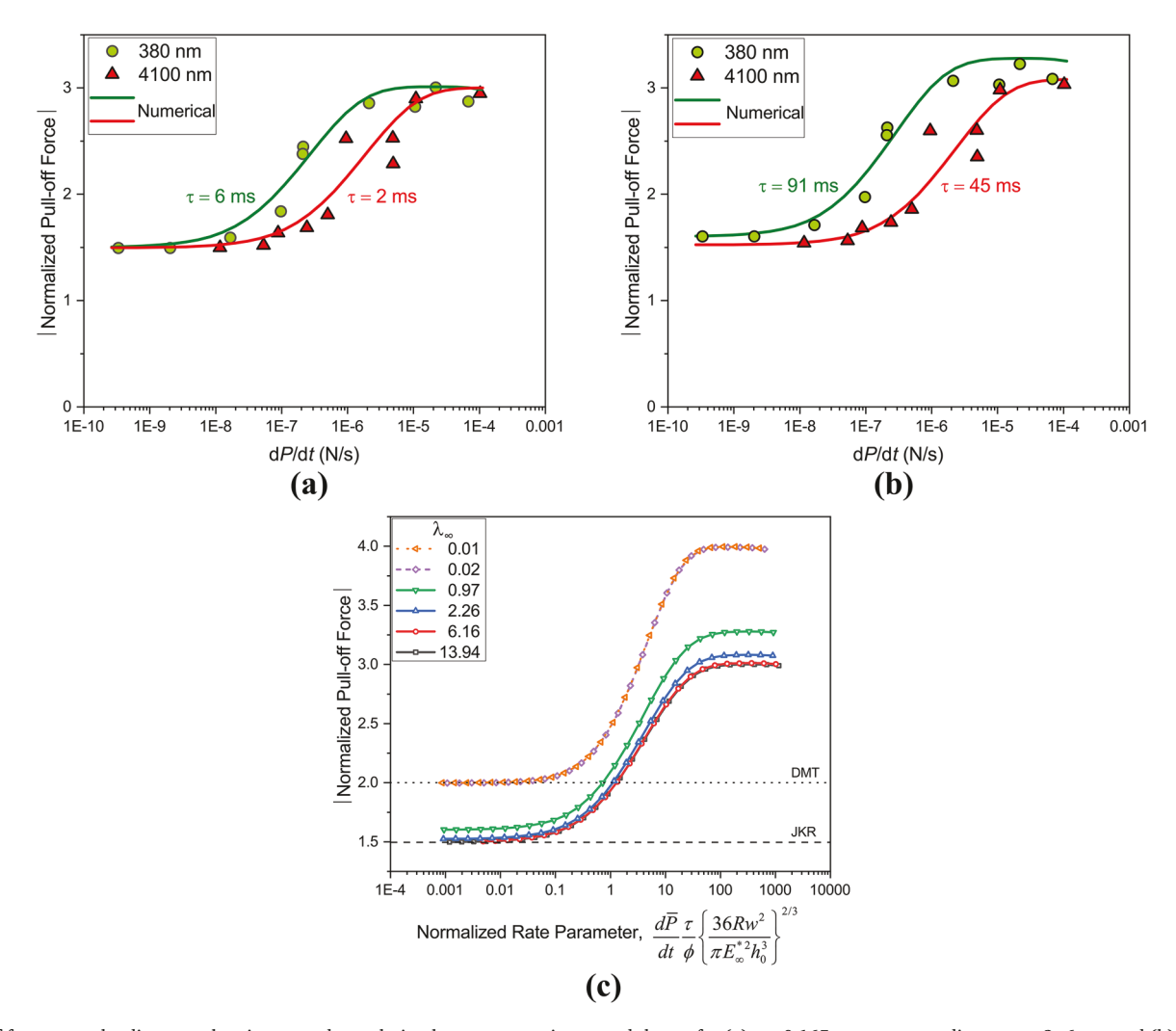


Fig. 6. Normalized pull-off force vs. unloading rate showing a good correlation between experiment and theory for (a) z_0 =0.165 nm corresponding to τ =2-6 ms, and (b) z_0 =1 nm corresponding to τ =45-90 ms. (c) Dependence of the *S*-shaped curves on the Maugis parameter, λ_{∞} . The normalized pull-off force increases with decreasing λ_{∞} . For slow unloading rates, the normalized pull-off force increases from 1.5 (JKR) to 2 (DMT), while for fast unloading rates the normalized pull-off increases from 3 (JKR) to 4 (DMT) for k = 0.5. (For interpretation of the references to color in this figure, the reader is referred to the web version of this article.)

of $d_{pull-off}$ from the numerical simulation (Section 3.5.1). The four *S*-shaped curves plotted with solid lines in Fig. 6(c) are valid for the model developed in this work for $\lambda_{\infty} \ge 1$. The curves demonstrate an increase in the normalized pull-off force with decreasing λ_{∞} . If the assumption by Barthel and Roux (2000) (Section 3.4.1) is considered as valid, the current M-D viscoelastic model could be extended to the DMT limit that is represented by dashed lines in Fig. 6(c), for the cases of $\lambda_{\infty} = 0.01$ and $\lambda_{\infty} = 0.02$. Furthermore, the normalized pull-off force has the following two limits at the extremes of the rate parameter: For slow detachment rate parameters: $\psi \to 1.5$ (JKR: $\lambda_{\infty} > 5$) and $\psi \to 2$ (DMT: $\lambda_{\infty} < 0.1$) (Eq. (1)), and for fast detachment rate parameters: $\psi/k \to 3$ (JKR) and $\psi/k \to 4$ (DMT).

4. Conclusions

The rate dependent adhesion of viscoelastic polymer nanofibers interacting through strong van der Waals forces was investigated via a coupled experimental/theoretical approach. The experiments were carried out via a recently developed method for normal and shear detachment experiments between individual nanofibers, which utilizes precision MEMS force sensors. It was shown that the apparent work of adhesion of PAN fibers, as calculated from the pull-off force in normal detachment experiments, increases with the rate of unloading by a factor of two within a three orders of magnitude increase in the unloading rate. The M-D contact model was extended to account for viscoelastic dissipation, which provided a good fit of the experimental normal pull-off force vs. unloading rate data. The extended M-D contact model for a standard linear solid with extracted time constants τ =2-6 ms (z_0 =0.165 nm) or τ =45-90 ms (z_0 =1 nm), captured well the experimental results for two fiber diameters that differed by an order of magnitude. This study provides new perspectives into the rate-dependent adhesion of soft fibers interacting with strong van der Waals forces, with direct implications in the way energy dissipation in natural/artificial fibrous systems is treated, as well as the design of strong and tough networks of soft fibers and their composites.

CRediT authorship contribution statement

Debashish Das: Conceptualization, Methodology, Software, Validation, Formal analysis, Investigation, Writing – original draft, Writing – review & editing, Visualization. **Ioannis Chasiotis:** Conceptualization, Methodology, Writing – review & editing, Supervision, Project administration, Funding acquisition, Data curation.

Declaration of Competing Interest

None.

Acknowledgments

The authors acknowledge the support by the National Science Foundation through CMMI grants #1635681 and #2022471. The FIB, and SEM studies were carried out at the Frederick Seitz Materials Research Laboratory Central Research Facilities, University of Illinois.

References

```
Barthel, E., Frétigny, C., 2009. Adhesive contact of elastomers: effective adhesion energy and creep function. J. Phys. D Appl. Phys. 42 (19), 195302.
Barenblatt, G.I., 1962. The mathematical theory of equilibrium cracks in brittle fracture. Adv. Appl. Mech. 7, 55-129. Vol.
Barthel, E., Roux, S., 2000. Velocity-dependent adherence: an analytical approach for the JKR and DMT models. Langmuir 16 (21), 8134-8138.
Barthel, E., 1998. On the description of the adhesive contact of spheres with arbitrary interaction potentials. J. Colloid Interface Sci. 200 (1), 7-18.
Das, D., Chasiotis, I., 2020. Sliding of adhesive nanoscale polymer contacts. J. Mech. Phys. Solids 140, 103931.
Derjaguin, B.V, Muller, V.M, Toporov, Y.P., 1975. Effect of contact deformations on the adhesion of particles. J. Colloid Interface Sci. 53 (2), 314-326.
Dugdale, D.S., 1960. Yielding of steel sheets containing slits. J. Mech. Phys. Solids 8 (2), 100-104.
Graham, G.A.C., 1967. The contact problem in the linear theory of viscoelasticity when the time dependent contact area has any number of maxima and minima. Int.
   J. Eng. Sci. 5 (6), 495-514.
Greenwood, J.A., Johnson, K.L., 1998. An alternative to the Maugis model of adhesion between elastic spheres. J. Phys. D Appl. Phys. 31 (22), 3279.
Greenwood, J.A., Johnson, K.L., 2006. Oscillatory loading of a viscoelastic adhesive contact. J. Colloid Interface Sci. 296 (1), 284-291.
Greenwood, J.A., Johnson, K.L., 1981. The mechanics of adhesion of viscoelastic solids. Philos. Mag. A 43 (3), 697-711.
Hui, C.Y., Baney, J.M., Kramer, E.J., 1998. Contact mechanics and adhesion of viscoelastic spheres. Langmuir 14 (22), 6570-6578.
Israelachvili, J.N., 2015. Intermolecular and Surface Forces. Academic press.
Israelachvili, J.N., Tabor, D., 1972. The measurement of van der Waals dispersion forces in the range 1.5 to 130 nm. Proc. R. Soc. Lond. A Math. Phys. Sci. 331 (1584),
Johnson, K.L., Kendall, K., Roberts, A.D., 1971. Surface energy and the contact of elastic solids. Proc. R. Soc. Lond. A 324 (1558), 301-313.
Johnson, K.L., 1999. Contact mechanics and adhesion of viscoelastic spheres. ACS Symp. Ser. 741, 24-41.
Johnson, K.L., Greenwood, J.A., 2002. Adhesion of viscoelastic spherical solids. Contact Mechanics. Springer, Dordrecht, pp. 141–160.
Knauss, W.G., 1970. Delayed failure—the Griffith problem for linearly viscoelastic materials. Int. J. Fract. Mech. 6 (1), 7-20.
Liu, J., Das, D., Yang, F., Schwartz, A.G., Genin, G.M., Thomopoulos, S., Chasiotis, I., 2018. Energy dissipation in mammalian collagen fibrils: cyclic strain-induced
    damping, toughening, and strengthening. Acta Biomater. 80, 217-227.
Liechti, K.M., Wu, J.D., 2001. Mixed-mode, time-dependent rubber/metal debonding. J. Mech. Phys. Solids 49 (5), 1039–1072.
Li, L., Mangipudi, V.S., Tirrell, M., Pocius, A.V., 2001. Direct measurement of surface and interfacial energies of glassy polymers and PDMS. Fundamentals of
    Tribology and Bridging the Gap Between the Macro-and Micro/Nanoscales. Springer, Dordrecht, pp. 305-329.
Lorenz, B., Krick, B.A., Mulakaluri, N., Smolyakova, M., Dieluweit, S., Sawyer, W.G., Persson, B.N.J., 2013. Adhesion: role of bulk viscoelasticity and surface
    roughness. J. Phys. Condens. Matter 25 (22), 225004.
```

Maugis, D., 1992. Adhesion of spheres: the JKR-DMT transition using a Dugdale model. J. Colloid Interface Sci. 150 (1), 243-269.

Maugis, D., Barquins, M., 1978. Fracture mechanics and the adherence of viscoelastic bodies. J. Phys. D Appl. Phys. 11, 1989-2023.

Maeda, N., Chen, N., Tirrell, M., Israelachvili, J.N., 2002. Adhesion and friction mechanisms of polymer-on-polymer surfaces. Science 297 (5580), 379–382.

Naraghi, M., Kolluru, P.V., Chasiotis, I., 2014. Time and strain rate dependent mechanical behavior of individual polymeric nanofibers. J. Mech. Phys. Solids 62, 257–275

Naraghi, M., Chasiotis, I., Kahn, H., Wen, Y., Dzenis, Y., 2007. Mechanical deformation and failure of electrospun polyacrylonitrile nanofibers as a function of strain rate. Appl. Phys. Lett. 91 (15), 151901.

Naraghi, M., Ozkan, T., Chasiotis, I., Hazra, S.S., De Boer, M.P., 2010. MEMS platform for on-chip nanomechanical experiments with strong and highly ductile nanofibers. J. Micromech. Microeng. 20 (12), 125022.

Naraghi, M., Chasiotis, I., Kahn, H., Wen, Y., Dzenis, Y., 2007. Novel method for mechanical characterization of polymeric nanofibers. Rev. Sci. Instrum. 78 (8), 085108

Negi, V., Picu, R.C., 2019. Mechanical behavior of nonwoven non-crosslinked fibrous mats with adhesion and friction. Soft Matter 15 (29), 5951-5964.

Papangelo, A., Ciavarella, M., 2019. On mixed-mode fracture mechanics models for contact area reduction under shear load in soft materials. J. Mech. Phys. Solids 124, 159–171.

Schapery, R.A., 1975. A theory of crack initiation and growth in viscoelastic media. Int. J. Fract. 11 (1), 141-159.

Schapery, R.A., 1975. A theory of crack initiation and growth in viscoelastic media II. Approximate methods of analysis. Int. J. Fract. 11 (3), 369-388.

Schapery, R.A., 1989. On the mechanics of crack closing and bonding in linear viscoelastic media. Int. J. Fract. 39 (1-3), 163-189.

Shi, Q., Wan, K.T., Wong, S.C., Chen, P., Blackledge, T.A., 2010. Do electrospun polymer fibers stick? Langmuir 26 (17), 14188-14193.

Shi, Q., Wong, S.C., Ye, W., Hou, J., Zhao, J., Yin, J., 2012. Mechanism of adhesion between polymer fibers at nanoscale contacts. Langmuir 28 (10), 4663–4671. Shrestha, R., Cai, J., Naraghi, M., de Boer, M.P., 2020. Size-dependent creep master curve of individual electrospun polymer nanofibers. Exp. Mech. 60, 763–773.

Stachewicz, U., Hang, F., Barber, A.H., 2014. Adhesion anisotropy between contacting electrospun fibers. Langmuir 30 (23), 6819-6825.

Ting, T.C.T., 1966. The contact stresses between a rigid indenter and a viscoelastic half-space. ASME, J. Appl. Mech. 33, 845–854.

Waters, J.F., Guduru, P.R., 2010. Mode-mixity-dependent adhesive contact of a sphere on a plane surface. Proc. R. Soc. A Math. Phys. Eng. Sci. 466 (2117), 1303–1325.

Wang, X., Najem, J.F., Wong, S.C., Wan, K.T., 2012. A nano-cheese-cutter to directly measure interfacial adhesion of freestanding nano-fibers. J. Appl. Phys. 111 (2), 024315.

Wang, X., Wong, S.C., Jung, Y.J., Wan, K.T., 2017. Measuring interfacial adhesion of carbon nanotube bundles and electrospun polymer fibers. Langmuir 33 (44), 12592–12595.

Zeng, H., Maeda, N., Chen, N., Tirrell, M., Israelachvili, J., 2006. Adhesion and friction of polystyrene surfaces around Tg. Macromolecules 39 (6), 2350-2363.